The Astrophysical Journal, 678:1279–1291, 2008 May 10

REACHING THE END OF THE WHITE DWARF COOLING SEQUENCE IN NGC 6791[1]

Luigi R. Bedin,[2] Ivan R. King,[3] Jay Anderson,[2,4] Giampaolo Piotto,[5]
Maurizio Salaris,[6] Santi Cassisi,[7] and Aldo Serenelli[8]
Received 2007 October 19; accepted 2007 December 19

ABSTRACT

We present new observations of the white dwarf sequence of the old open cluster NGC 6791. The brighter peak previously observed in the white dwarf luminosity function (WDLF) is now better delineated, and the second, fainter peak that we suggested earlier is now confirmed. A careful study suggests that we have reached the end of the WD sequence. The WDs that create the two peaks in the WDLF show a significant turn to the blue in the color-magnitude diagram. The discrepancy between the age from the WDs and that from the main-sequence turnoff remains, and we have an additional puzzle in the second peak in the WDLF. Canonical WD models seem to fail—at least at $\sim$25% level—in reproducing the age of clusters of this metallicity. We discuss briefly possible ways of arriving at a theoretical understanding of the WDLF.

Subject headings: open clusters and associations: individual (NGC 6791) — white dwarfs
Online material: color figures

1. INTRODUCTION

NGC 6791 is a very unusual open cluster. It is one of the richest (an unpublished star count by one of us [I. R. K.] shows about 3000 cluster stars brighter than $B \sim 21$); it is old ($\sim$8 Gyr) and very metal-rich ([Fe/H] $\sim +0.4$; Gratton et al. 2006; Carraro et al. 2006; Origlia et al. 2006). Furthermore, it is close enough that *Hubble Space Telescope* Advanced Camera for Surveys (*HST* ACS) imaging can reach to very faint luminosities. The original aim of our program (GO 9815 and 10471; PI: I. R. King) was to study the bottom of the main sequence (MS; King et al. 2005), and we plan to use the new observations presented here to study the MS down to the hydrogen-burning limit. However, our first look at the color-magnitude diagram (CMD) had made it clear that the white dwarf cooling sequence (WDCS) was even more exciting than the bottom of the MS (Bedin et al. 2005a). The WDCS presented in that study suggested an age much smaller than the MS turnoff (TO) age.

The purpose of the present paper is to extend the WD sequence to fainter magnitudes by adding a new set of *HST* ACS images acquired since the previous result was published. We will show that our new data set is deep enough to reveal the second, fainter peak in the WD luminosity function (LF) that was hinted at by Bedin et al. (2005a), and that the WDCS is truncated just below this second peak.

2. OBSERVATIONS AND MEASUREMENTS

2.1. *Observational Data*

The Bedin et al. (2005a) study was based on only one epoch of data. Here we add a second epoch, and also introduce improvements in the reduction procedures.

Both epochs were taken with the Wide Field Channel (WFC) of ACS. The first-epoch images (GO 9815) were taken on 2003 July 16, and consisted of the following exposures: F606W, 4×1185 s $+ 2 \times 1142$ s $+ 3 \times 30$ s; F814W, 4×1185 s $+ 2 \times 1142$ s $+ 3 \times 30$ s. Our second-epoch exposures (GO 10471), which were taken on 2005 July 13, had been planned before we realized how interesting and accessible the WDCS would be; as a result our program was aimed at reaching as faint as we could on the MS. We therefore chose to repeat our observations only in the F814W filter, in order to improve our photometric precision for the lower MS stars and to obtain proper motions to separate them from the field stars. The GO 10471 exposures were 4×1264 s $+ 2 \times 1200$ s $+ 3 \times 30$ s. All our exposures (in both epochs) were well dithered.

To strengthen our measurements of the brighter stars, we also measured archival images taken in GO 10265 (PI: T. Brown); these consisted of *HST* ACS exposures, in each of F606W and F814W, of 0.5, 5, and 50 s, without dithering. These images overlap about half of our field. Since their role is only to extend our sparse sampling of the upper parts of the CMD, they were not used for the WDs, but only to study the MS TO.

2.2. *Measurements and Reduction*

Since our two previous papers on NGC 6791 (Bedin et al. [2005a] for the WDCS and King et al. [2005] for the MS), our methods of measurement and reduction have evolved and improved. The software program used to find and measure stars is described in detail in Anderson et al. (2008). Here we summarize briefly what the program does.

The first step of all is to construct for each filter a 9×10 array of point-spread functions (PSFs) that correctly represent the spatial variation of the ACS WFC PSF, along with, for each individual image, what Anderson & King (2006, hereafter AK06) call a perturbation PSF for that image. The function of the latter

---

[1] Based on observations with the NASA/ESA *Hubble Space Telescope*, obtained at the Space Telescope Science Institute, which is operated by AURA, Inc., under NASA contract NAS 5-26555.

[2] Space Telescope Science Institute, 3800 San Martin Drive, Baltimore, MD 21218; bedin@stsci.edu.

[3] Department of Astronomy, University of Washington, Box 351580, Seattle, WA 98195-1580; king@astro.washington.edu.

[4] Department of Physics and Astronomy, MS-108, Rice University, 6100 Main Street, Houston, TX 77005; jayander@stsci.edu.

[5] Dipartimento di Astronomia, Università di Padova, Vicolo dell'Osservatorio 2, I-35122 Padua, Italy; giampaolo.piotto@unipd.it.

[6] Astrophysics Research Institute, Liverpool John Moores University, 12 Quays House, Birkenhead CH41 1LD, UK; ms@astro.livjm.ac.uk.

[7] INAF–Osservatorio Astronomico di Collurania, Via M. Maggini, 64100 Teramo, Italy; cassisi@oa-teramo.inaf.it.

[8] Institute for Advanced Study, Einstein Drive, Princeton, NJ 08540; aldos@ias.edu.

is to account for focus changes related to the particular breathing state of the telescope during that exposure.

The data are reduced in two separate passes. The first-pass reduction uses the code described in AK06 to find the relatively bright stars, and measure positions and fluxes for them. We then use these star lists to find the six-parameter linear transformations from the coordinates in any image (after correction for geometrical distortion) to those in a distortion-free reference frame, and also to put the magnitudes into a common zero-point system. In doing this we use only stars with solid and consistent detection in all the exposures. Here, as in the second pass, all measurements are made on the `flt` images, which have been flat fielded and bias subtracted, but have not been resampled.

The procedures of the second pass are quite different from those of the first pass. First, we restrict the analysis to one small 25×25 pixel patch of the field at a time, going through systematically in a mosaic fashion, so as to cover the whole field. Each patch is specified by the coordinates of its center in the reference frame, and we use the transformations to identify the location of the center of the patch in each of the individual exposures, from which we extract a 25×25 raster centered on this location. By "the individual exposures" we mean all the exposures in either filter.

A sophisticated software routine then uses the rasters from all of the individual exposures to find the brightest sources and to measure a single position and an F606W and an F814W flux for each one, using all the exposures simultaneously. It then subtracts out the newfound sources from each exposure and iterates the finding procedure until no more objects are found. To qualify as found, our automated routines required that an object be detected in at least seven out of the 18 images, and in addition, we required these objects to be detected in a minimum of two of the six F606W and two of the 12 F814W deep images.

In order to avoid identifying PSF features as stars, we constructed a generous upper limit model of the extended PSF, including the diffraction spikes, in such a way as to allow everywhere for the largest upward excursions that each PSF pixel might reasonably make, and we insisted that any faint star in the vicinity of a bright star must be brighter than any PSF feature that could be present. This procedure does an excellent job of keeping PSF features out of our lists, and ends up excluding very few legitimate stars.

In addition to solving for positions and fluxes during the simultaneous fitting process above, we also compute a very important image shape parameter for each source: RADXS. This is a measure of how much flux there is in the pixels just outside of the core, in excess of the prediction from the PSF. (We measure it using the pixels between $r = 1.0$ and $r = 2.5$, and it is reported relative to the star's total flux.) RADXS is positive if the object is broader than the PSF, and negative if it is sharper. This quantity is of great importance in distinguishing between stars and galaxies whose images are nearly as sharp; the latter are especially numerous in the part of the CMD where the faint WDs lie. We experimented with several similar diagnostic parameters and found that RADXS affected the best star-galaxy separation for this data set.

For each patch, we compute a stacked representation of the scene in a manner similar to Drizzle (Fruchter & Hook 2002) with `pixfrac` = 0. This stack is free of cosmic rays and image artifacts. We use this stack to compute two other important parameters for each detected object; these are the local sky background (SKY) and its rms deviation (rmsSKY). These parameters are computed by taking the stack pixels in the annulus between 3.5 and 8.0 pixels from the central pixel of the star, and calculating their mean and the rms deviation from the mean. There is no sigma clipping done, since we want to be sensitive to all the background noise that is present. The need for the SKY value is obvious; as for rmsSKY, we will explain below how it gives us a useful indication of how difficult the local background may make it to measure faint stars.

Artificial star (AS) tests are done using a similar patch-based procedure. For each AS, a position and an F606W magnitude are chosen in a random way; the F814W magnitude is then chosen so that the star's color puts it on the ridgeline of the WD sequence. We next extract from each exposure a patch centered on the AS location. The AS is added into the raster for each exposure at the appropriate location, in the form of an appropriately scaled PSF with Poisson noise. The software routine then operates blindly on the patch, finding and measuring all the stars. We examine the resulting list of sources to see if the AS was recovered. The ASs are used, it should be noted, not only as a measure of completeness; they also serve, at a number of stages of the procedure, to help develop and calibrate our criteria for choice of valid stars.

2.3. *Photometric Zero Points*

We calibrate the photometry to the WFC ACS Vega-mag system following the procedure given in Bedin et al. (2005b), and using the encircled energy and the zero points given by Sirianni et al. (2005). Given the high background ($\sim$65 e^- pixel^{-1}) in these exposures, we would not expect much of a charge transfer efficiency (CTE) correction to be necessary. Nonetheless we did compare the photometry of the two epochs; since CTE increases linearly with time (Riess & Mack 2004), any CTE losses should be about twice as large in the second epoch as in the first. We plotted $m_2 - m_1$ against the y-coordinate and saw no trends, indicating that any CTE present is much smaller than the random photometric errors.

3. SELECTION OF STARS

By using stacked images to examine stars from our lists, we found that our automated finding algorithm had successfully identified all of the faint stars that we might find by eye, and it had also successfully avoided identifying PSF features as stars. But the automated procedure had included in its list many barely resolved galaxies.

It is particularly important to identify these galaxies, because they fall in the part of the CMD where the faint end of the WD sequence lies. To distinguish these barely resolved objects from point sources, we use the shape parameter RADXS, which measures any excess flux just outside of the PSF core. Here the ASs are very instructive, since they show us how RADXS should behave with magnitude for true point sources. Figure 1 shows us the trend of RADXS against magnitude (for each filter) for ASs on the right of each panel, and on the left for stars that we consider (thus far) to be real. It is clear that many of the objects that we have thus far included as stars are far more extended than are the ASs, which we know have truly stellar profiles because we made them that way. We use the distributions for the ASs to mark out boundaries in these diagrams that should retain nearly all the objects that are truly stars; they are indicated by the gray lines, which were drawn in each AS panel in such a way as to include almost all of the recovered stars; they are repeated identically in the corresponding real star panel. (We believe that the tail-off of objects to the right in the AS panels is produced by star-star blends, which certainly should be eliminated from our photometry.)

Our second image quality parameter, rmsSKY, hardly figures in the direct selection of stars, but it does tell us how suitable the surroundings of each star are for good photometry. An unusually

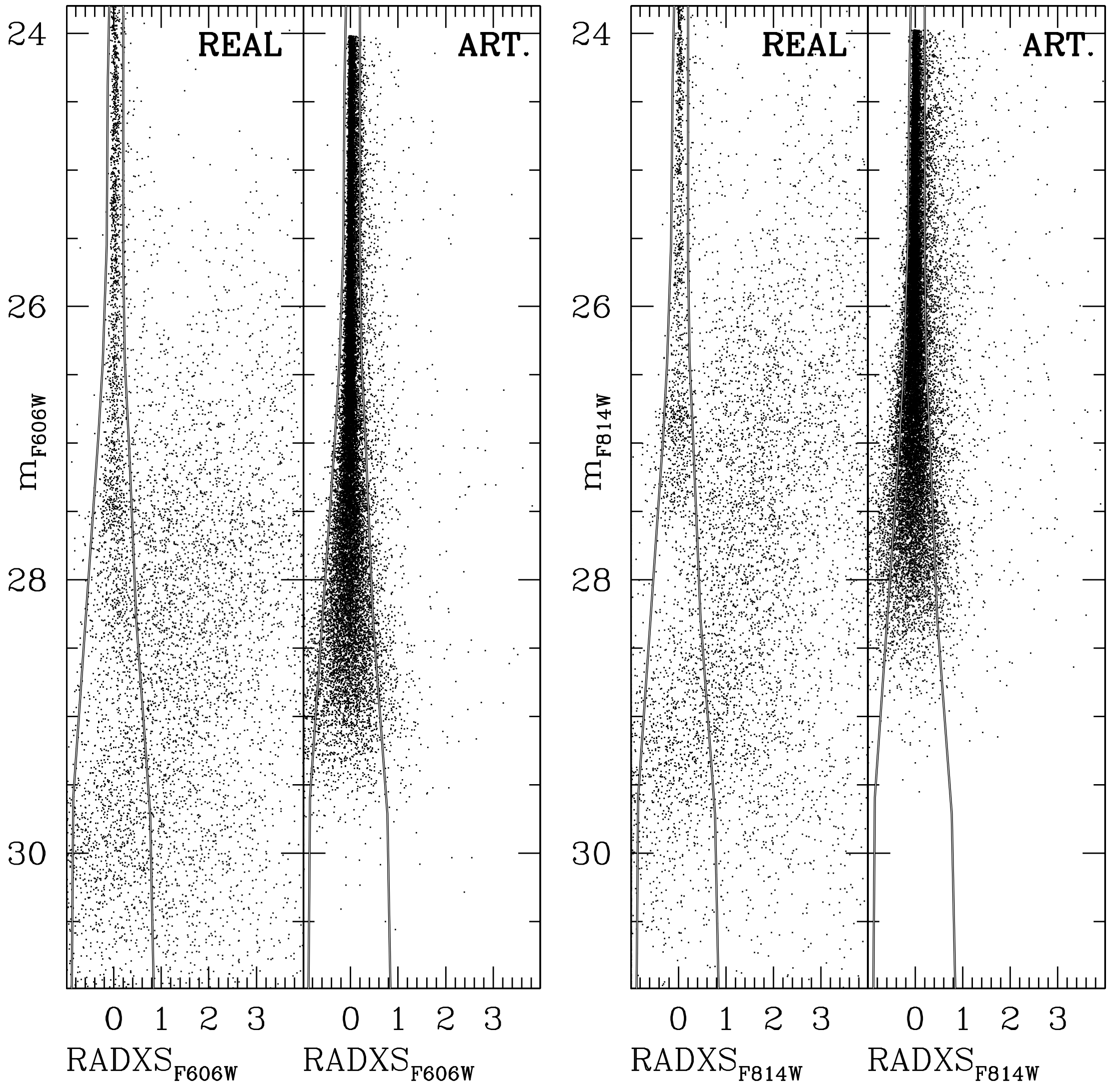

Fig. 1.—Parameter RADXS as a function of magnitude for ASs and real detections, in filter F606W (*left*) and in filter F814W (*right*). Detections between the two gray lines are considered real stars. Note how the real stars peter out at a much brighter magnitude than the artificial ones (particularly in the F814W filter).

high value of rmsSKY indicates a region where the background is irregular—often caused by the mottled halo of a bright star's PSF. We say "unusually high" rather than just "high" because even in the absence of interfering objects, rmsSKY will increase with the brightness of the star around which it is measured; because it must be measured only a few pixels from the star, its value has an increase that comes from the PSF wings of the star image around which it is measured. The value of SKY in the measuring annulus goes up, and its Poisson noise increases the value of rmsSKY. This effect is clearly seen in Figure 2, which displays rmsSKY for real and ASs in the two filters in a way exactly analogous to the way Figure 1 displayed RADXS. Again, limit lines have been drawn by eye for the ASs, in a way that distinguishes the large majority of normal cases from the small proportion of disturbed ones. The same limiting lines, when applied to the real stars, served to eliminate those stars whose photometry is suspect because of irregularity of their background. We will use rmsSKY again in § 4, where it plays an even more important role.

Figure 3 shows the WD region of the CMD of NGC 6791, with various selection criteria: first all objects that were measured at all, then all stars that were measured in at least two deep images for each filter, next the survivors when only the rmsSKY criterion is used for selection, then all the objects that met the RADXS criterion, and finally the stars that qualified with respect to both RADXS and rmsSKY. Since the last two panels are nearly identical, it is clear that rmsSKY removes very few objects that were not already removed by RADXS.

The WDCS that we find here for NGC 6791 is consistent with the one exhibited by Bedin et al. (2005a), and the second peak, which was hinted at in their diagram, is now quite clear.

4. COMPLETENESS

The ASs were carried through all the stages of the measurement procedure in exactly the same way as the real stars, so as a measure of completeness we simply counted the fraction of ASs that were recovered, as a function of magnitude. We considered an AS to be recovered if its measured position was within 0.75 pixels and its magnitude within 0.5 mag of the input values, for both filters.

This is a simple and straightforward approach to completeness, and it does indeed provide the correct factor, as a function of magnitude, by which to divide the observed numbers in order to derive completeness-corrected numbers. There is great value, however, in looking at completeness in a more detailed way. For faint stars our numbers are less complete for two reasons. One is simply

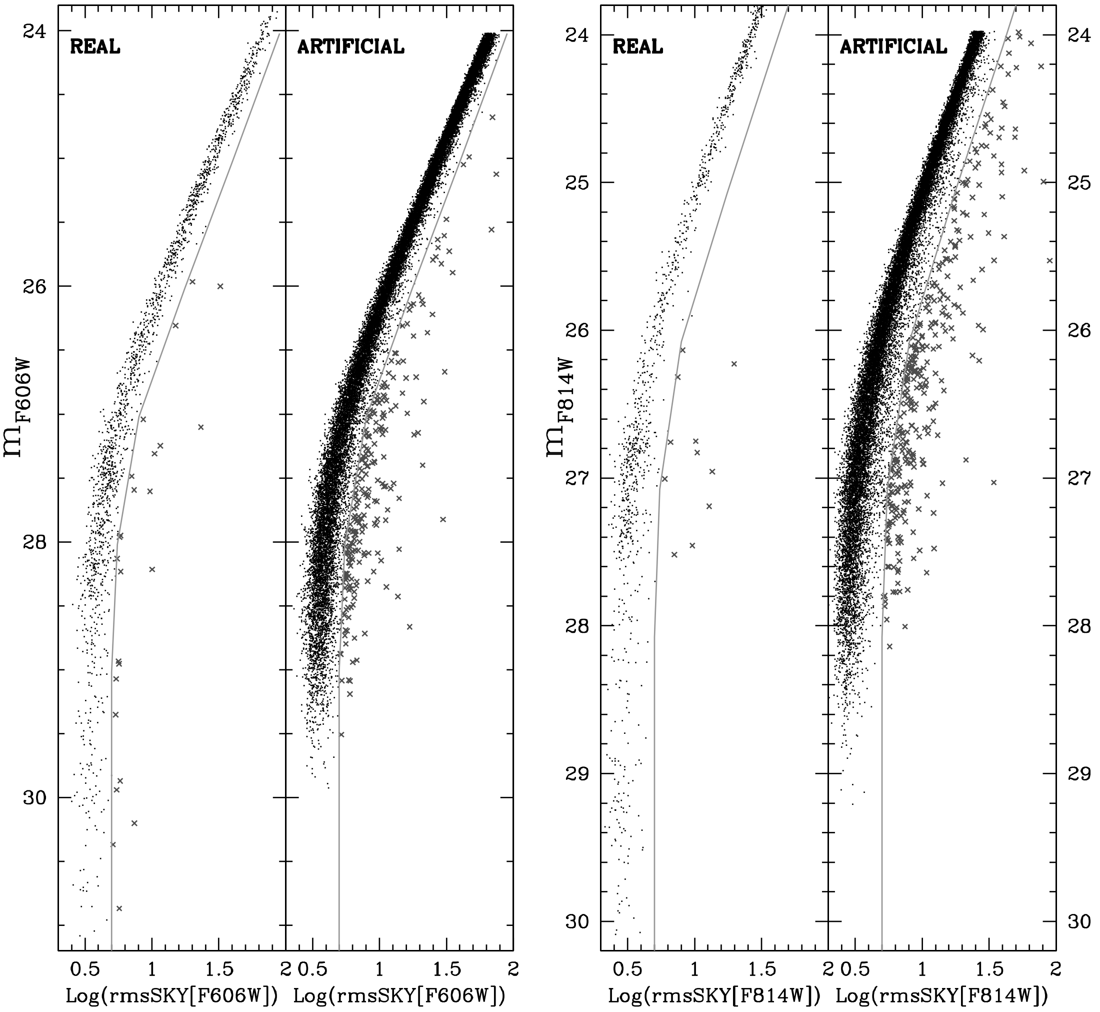

Fig. 2.—Only stars that passed the RADXS selection shown in this figure. We plot here the $\log_{10}$ of the rmsSKY parameter as a function of magnitude, for both ASs and real detections, in filter F606W (*left*) and in filter F814W (*right*). Stars with rmsSKY to the left of the thin line are likely to be well measured. The others, plotted as crosses, are rejected. [*See the electronic edition of the Journal for a color version of this figure.*]

the difficulty of detecting faint stars. Even under the best of circumstances we will lose some fraction of the stars on account of statistical fluctuations that work against their detection. But a great deal of our loss of faint stars is for a quite different reason: there are regions of the image in which conditions are very unsuitable for the detection of faint stars; there is a quite appreciable fraction of the image area, in fact, in which even many of the bright stars are lost, because of interference by even brighter stars.

The distinction between these two possible reasons for missing stars becomes important when we consider the other application of the curve of completeness against magnitude: as a criterion of the reliability of the number of stars. It is customary to consider star numbers to be unreliable when the completeness figure has dropped below 50%. But which completeness? Imagine a field in which 60% of the total area is unsuitable for finding faint stars at all; the conventional completeness cannot be above 40% at any faint magnitude, and judging reliability from it would lead to the absurdity that there is no way to say anything about the faint population. Yet if we were to confine our measurements to that 40% of the field in which faint stars can be measured, we would correctly conclude that the star counts are reliable down to a fairly faint level.

Drawing the map of reliable areas—probably a quite complicated map—would be a daunting task, and this is where our rmsSKY parameter becomes so useful. The conventional completeness is $c = N_{\rm rec}/N_{\rm ins}$, where $N_{\rm ins}$ and $N_{\rm rec}$ are the numbers of stars inserted and recovered, respectively. But we can also define a good-region completeness, $c_g = N_{{\rm rec},\,g}/N_{{\rm ins},\,g}$; this is the completeness evaluated only in regions of low rmsSKY, where stars of that magnitude could be found without interference. The limit of reliability of our numbers is at the 50% level of c_g, not of c.

Figure 4 shows the completeness levels for our field. The 50% level of c is at F606W magnitude 28.05, while for c_g it is at 28.55. If we had followed the absurdity of using the 50% level of conventional completeness, instead of the informed choice of the 50% level of c_g, we would have lost the interval of half a magnitude that makes the difference between going deeper than the lower cutoff of the WDCS and failing to do so. Figure 4 also shows the fraction of the image area suitable for detection of faint sources (*open circles*).

5. PROPER MOTIONS

Here, to compute a proper motion for each star, we first measured a mean position for the star in the reference frame at each epoch, using all the exposures within that epoch. The proper motion, then, is the difference between the second- and first-epoch positions, divided by the baseline, and multiplied by the pixel scale (50 mas pixel^{-1}). The reference frame is aligned to have x and y parallel to right ascension and declination, respectively, so the proper motions are in a properly aligned frame as well. The

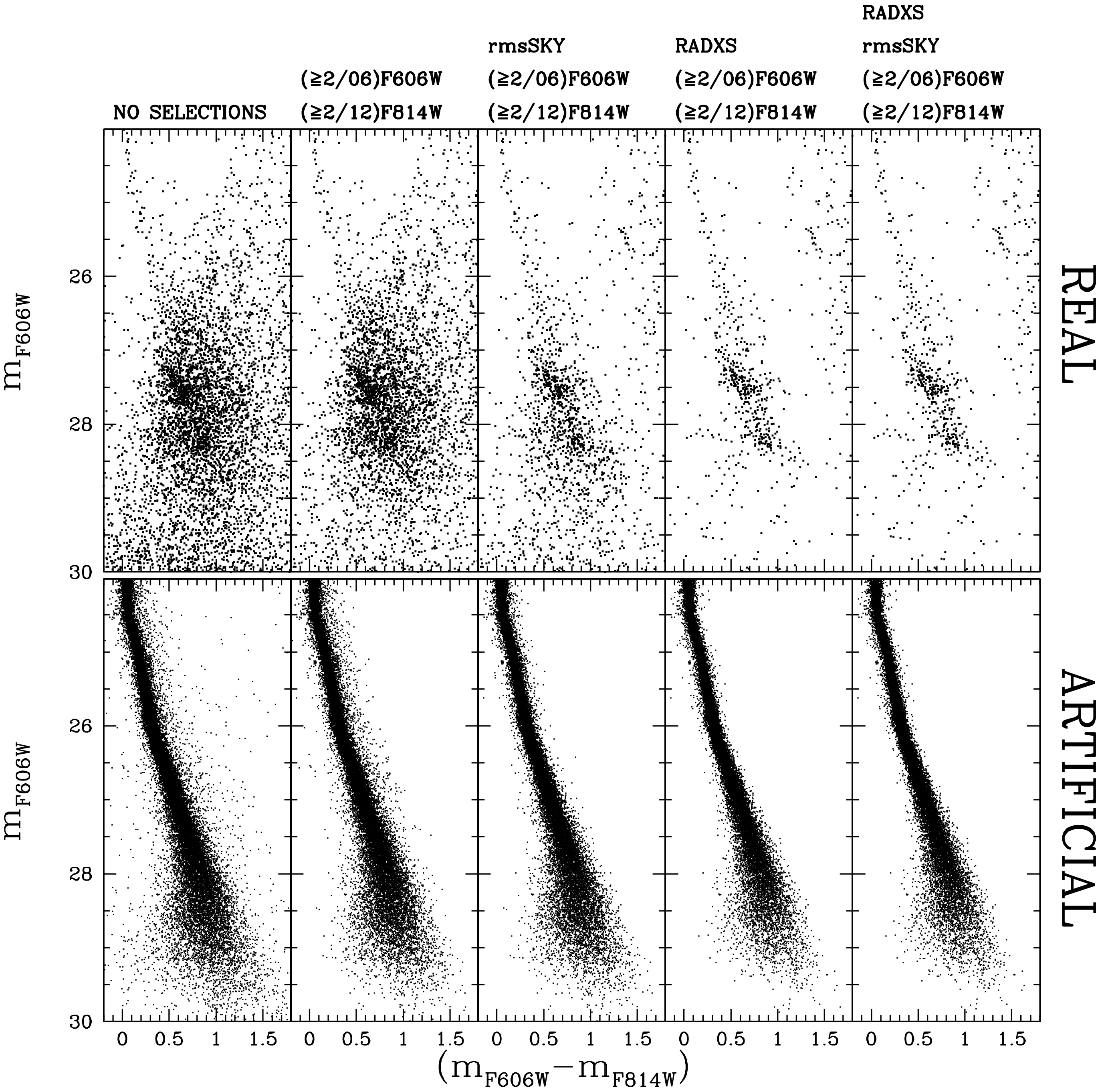

Fig. 3.—*Top*: The CMD of NGC 6791 with various selection criteria applied to the individual stars. *Bottom*: The same selection applied to the recovered ASs.

zero point of the motion is the cluster's bulk motion, since the reference frame was defined by member stars (Bedin et al. 2006).

Although our proper motions are very helpful for cleaning field stars from the upper MS part of the CMD and for the brighter WDs, for the faint WDs they turn out to be of very little use. This can be seen in Figure 5. For the brighter stars (*upper left*), the proper-motion precision easily allows us to separate the two populations. But as the stars get fainter, the proper motions become less accurate, the distributions for cluster and field overlap, and no accurate discrimination is possible. As is clear from the figure, there is a small difference between the mean proper motions of cluster and field stars, but by far the best discriminant is the very small dispersion of the motions of the cluster stars. It is equally clear from the figure that a clean separation would require a very much better accuracy in the motions of the faint stars—something that appears to be totally beyond our reach with the data sets that are available at present.

6. THE WHITE DWARF LUMINOSITY FUNCTION

Without a proper-motion elimination of field stars, the best we can do toward deriving a white dwarf luminosity function (WDLF) is to use the RADXS parameter to remove as many galaxies and artifacts as we can, and delimit in color the region of the CMD in which we consider stars to be WDs. For both of these tasks the AS experiments prove extremely useful. First, Figure 1 shows our treatment of the parameter RADXS. Independently for each filter, we used the AS tests to draw our discriminating lines, in such a way as to include nearly all legitimate objects; we then

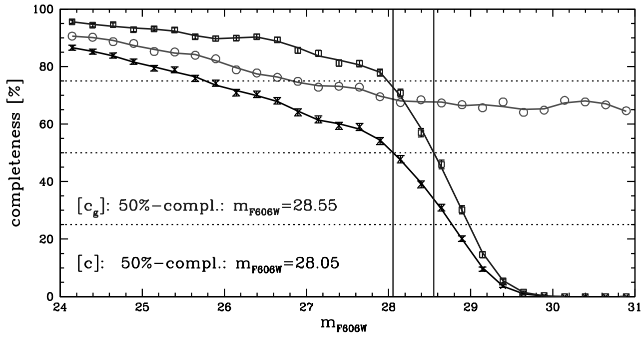

Fig. 4.—*Crosses*: Conventional completeness *c*. *Squares*: The low-rmsSKY completeness c_g that is defined in the text. *Circles*: Indicate the fraction of the image area where the bumpiness of the sky offers no impediment to finding a star, at each magnitude. The product of this curve and c_g is of course *c*. [*See the electronic edition of the Journal for a color version of this figure.*]

applied those same selection criteria to the real stars. A star was accepted only if it passed the RADXS test in both filters.

We then chose our boundaries in the CMD, as indicated in the second and fourth panels of Figure 6. The boundaries were chosen so that none of the ASs were lost, while the boundaries are set broadly enough to include all stars that might be WDs of some sort—including WD binaries, and unusual types of WDs.

In the central panel of Figure 6 is the completeness. According to the distinction made in § 4, we plot here the quantity *c*, which is the factor by which observed star numbers need to be divided in order to estimate the correct total. The horizontal line is the 50% completeness level of the quantity c_g, which, as we explained in § 4, is a realistic indicator of our ability to find stars in regions where interference does not prevent them from being found.

The rightmost panel of Figure 6 shows the WDLF. The observed numbers are indicated by a thin line histogram, and the completeness-corrected numbers are indicated by the thick line histogram. Error bars are shown only on the corrected values, but they are derived from the Poisson uncertainties in the observed values. The corresponding numbers are in Table 1. The LF below $m_{\rm F606W} = 28.55$ is highly suspect, both because of the low completeness and because the stars in this region show no coherence in color and are likely not to be WDs at all. For this reason that part of the LF is plotted with lines that are less heavy.

The WDLF obtained here very much resembles the one previously obtained by Bedin et al. (2005a; top panel of their Fig. 3), but we now see features that are somewhat better defined, as a

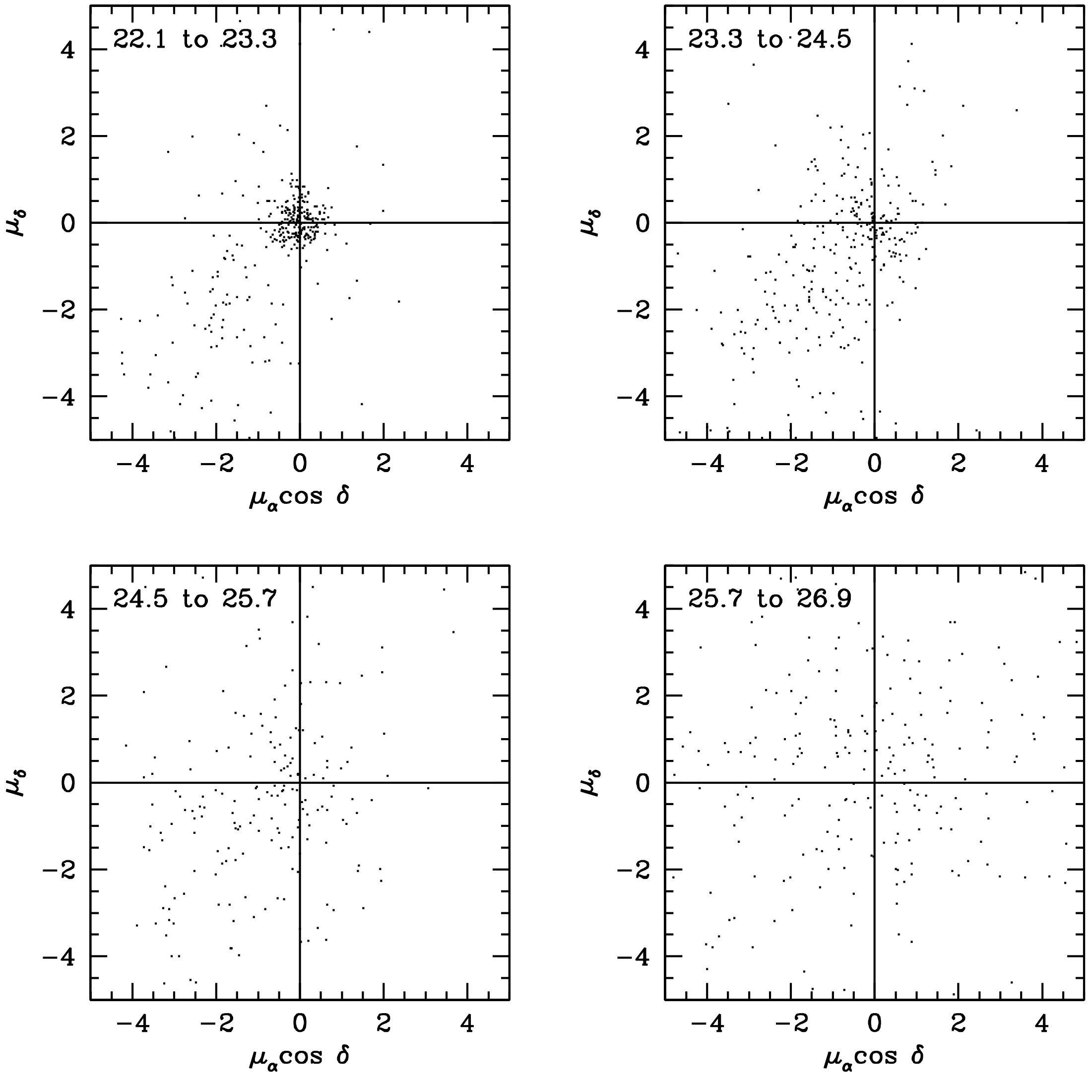

Fig. 5.—Proper motions for increasingly faint intervals of F814W magnitude. Zero point is the mean cluster motion. In the brightest interval the concentration of motions clearly identifies the cluster members, while field stars are more widely spread, and largely in the lower left-hand quadrant. At fainter magnitudes the measuring errors dominate, and no separation is possible.

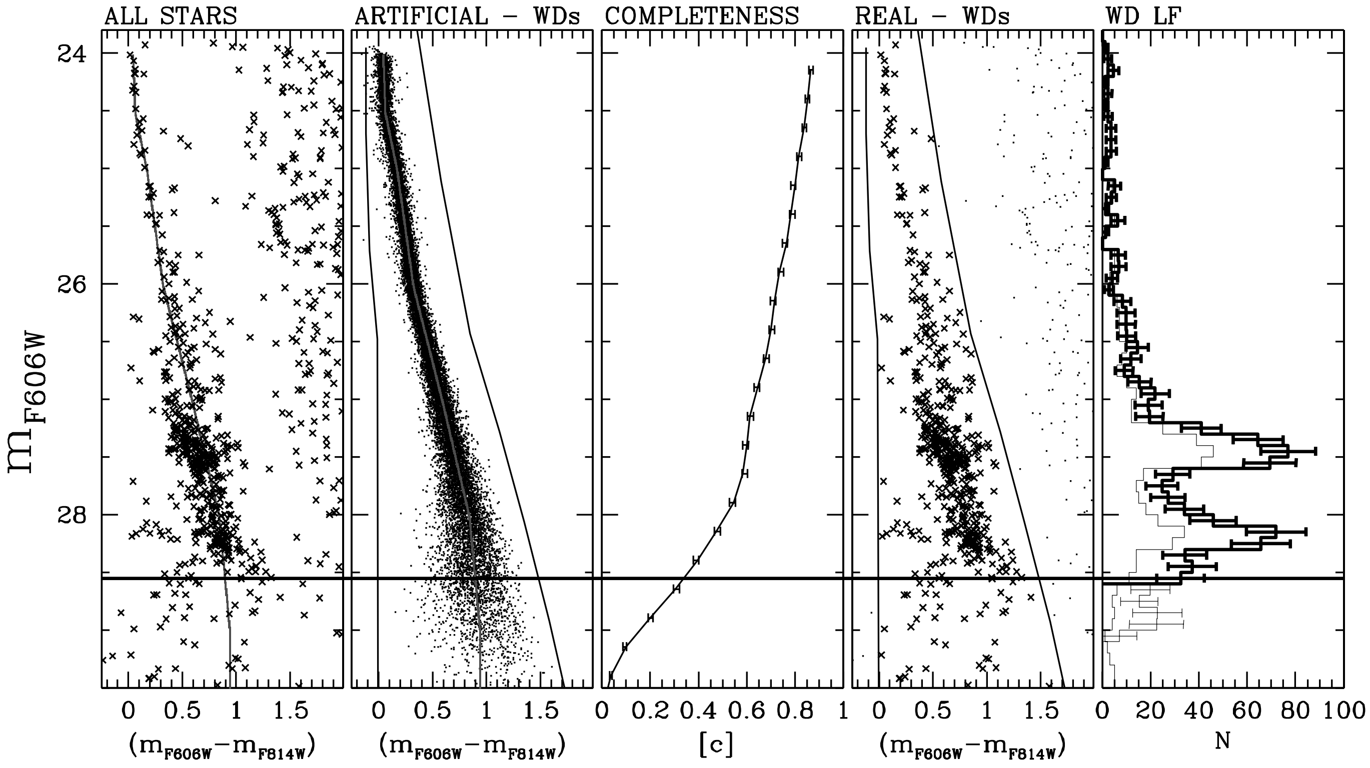

Fig. 6.—WDLF, including corrections for the completeness curve shown in the central panel. (Successive panels are observed CMD, ASs, completeness, selection of stars, and LF.) The horizontal line at magnitude 28.55 is the 50% completeness level of c_g. [*See the electronic edition of the Journal for a color version of this figure.*]

TABLE 1

Completeness-corrected WDLF

m_{F606W}	N_c	σ_{N_c}	m_{F606W}	N_c	σ_{N_c}
23.05.........	0.00	0.00	26.15.........	8.38	3.42
23.15.........	0.00	0.00	26.25.........	9.87	3.73
23.25.........	0.00	0.00	26.35.........	9.96	3.77
23.35.........	1.11	1.11	26.45.........	10.07	3.81
23.45.........	0.00	0.00	26.55.........	14.56	4.61
23.55.........	1.12	1.12	26.65.........	11.80	4.17
23.65.........	0.00	0.00	26.75.........	9.03	3.69
23.75.........	0.00	0.00	26.85.........	15.36	4.86
23.85.........	0.00	0.00	26.95.........	21.93	5.86
23.95.........	1.14	1.14	27.05.........	19.17	5.53
24.05.........	2.30	1.63	27.15.........	19.54	5.64
24.15.........	4.62	2.31	27.25.........	41.05	8.21
24.25.........	1.16	1.16	27.35.........	64.56	10.34
24.35.........	2.34	1.65	27.45.........	76.95	11.35
24.45.........	1.18	1.18	27.55.........	69.44	10.85
24.55.........	2.37	1.68	27.65.........	29.18	7.08
24.65.........	3.59	2.07	27.75.........	24.67	6.59
24.75.........	3.62	2.09	27.85.........	27.17	7.01
24.85.........	3.66	2.11	27.95.........	33.99	8.01
24.95.........	1.23	1.23	28.05.........	45.89	9.57
25.05.........	0.00	0.00	28.15.........	71.94	12.34
25.15.........	5.01	2.50	28.25.........	65.72	12.20
25.25.........	3.79	2.19	28.35.........	34.16	9.13
25.35.........	1.27	1.27	28.45.........	37.28	9.96
25.45.........	6.43	2.87	28.55.........	32.46	9.79
25.55.........	1.30	1.30	. . .	. . .	. . .
25.65.........	0.00	0.00	*28.65.........*	*19.87*	*8.11*
25.75.........	6.65	2.97	*28.75.........*	*15.36*	*7.68*
25.85.........	6.75	3.02	*28.85.........*	*22.85*	*10.22*
25.95.........	4.10	2.37	*28.95.........*	*22.44*	*11.22*
26.05.........	2.76	1.95	*29.05.........*	*7.22*	*7.22*

result of deeper integration in F814W and a more careful sample selection. The WDLF shows the expected mild rise down to $m_{F606W} \sim 27$, but then come the two unexpected peaks. (1) We confirm the presence of the first peak at a magnitude $m_{F606W} = 27.45 \pm 0.05$, better constrained than in our previous paper, and with a steeper drop than its rise—such as we might expect at the end of a cooling sequence. (2) But then there is a clear second peak, at magnitude $m_{F606W} = 28.15 \pm 0.05$.

We believe that the WDLF ends at a magnitude where our completeness is still reliable. This conclusion is strengthened by the CMD shown in the first and fourth panels of Figure 6, where any continuation of the LF is contributed by stars whose color is off that of the ridgeline of the WD sequence, so that they may well not be cluster WDs at all. AS tests indicate that if the WDCS continued below $m_{F606W} = 28.4$, we would see a well-defined sequence, as opposed to the sparse and scattered cloud that we do see, which certainly cannot correspond to a continuing sequence.

Finally, we note that at the magnitude levels of the two LF peaks, the WDs stand on the blue side of the cooling sequence in the CMD, forming a sort of blue hook. This feature is better seen in Figure 7, where we zoom around the fainter part of the WDCS, and it is expected from models (see next section). Note that the two blue hooks create the LF peaks.

At the time of writing (Bedin et al. 2005a), we estimated that the total number of observed WDs was consistent with the number to be expected from a Salpeter initial mass function (IMF) normalized to the present-day MF for MS stars (which we took from King et al. [2005]). We can now reexamine this question. Down to magnitude $m_{F606W} \sim 28.55$ we now observe 425 WDs that we assume to be NGC 6791 members; correction for incompleteness brings this to ~850. (We already commented that we do expect very few, if any, WDs below $m_{F606W} \sim 28.55$.) By contrast, the number of WDs expected from a Salpeter IMF normalized to the present-day MF is ~430. Using a Kroupa (2001)

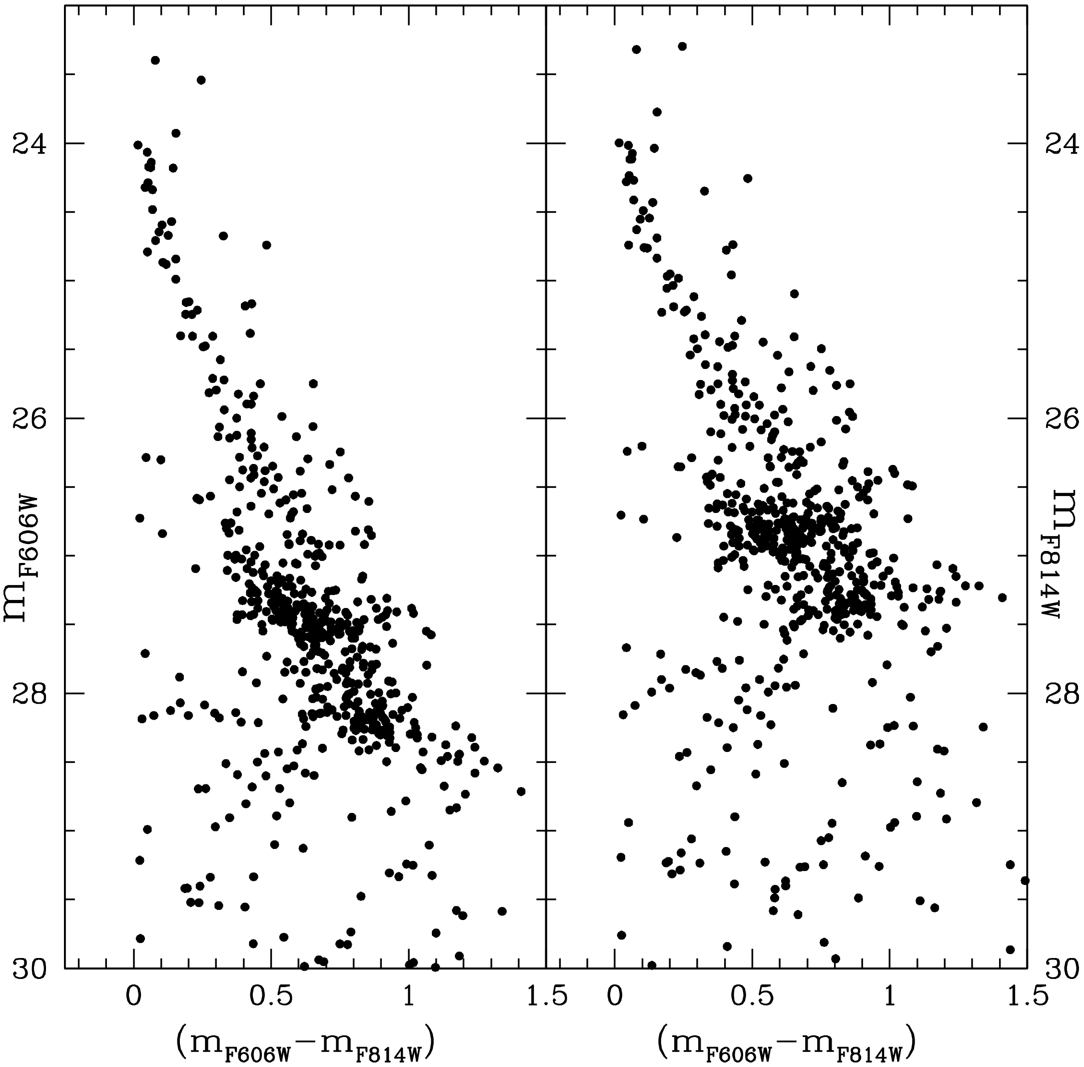

Fig. 7.—CMDs of the WDCS.

IMF we would expect ~500 WDs, still a factor of about 2 less than the measured counts.

We must treat these numbers with great reserve, however. They include no correction for background galaxies that may have been included in our WD count, although we expect it to be small because of the care we took in eliminating nonstellar objects (see § 3). We will return in § 7 to the question of contamination by background objects. As for the predicted number of WDs, it was calculated without taking into account the fact that our field lies completely within the core of the cluster, and it does not take mass segregation effects into account. Also, the assumption of a single slope for the power-law MF (or of a Kroupa 2001 MF) might be an oversimplification.

6.1. *Spatial Distribution of the WDs*

At the suggestion of the referee, we exhibit in this section the spatial distribution of the WDs in the two peaks of the LF. On the left side of Figure 8 we plot the WD CMDs and delineate with boxes the blue hook regions that contain nearly all of the stars in the two peaks. The horizontal line marks the 50% completeness limit for regions of low rmsSKY, as discussed in § 4. The right side of the figure shows the spatial distribution of all the objects above this completeness limit, with blue circles around the dots that represent stars in the upper rectangle and red squares for those in the lower rectangle. No differences are evident between the distributions of the red, the blue, and the plain dots.

7. CONTAMINATION BY BACKGROUND GALAXIES

There is clearly a danger that our supposed WD sample includes a number of sharp nuclei of background galaxies, as these objects have colors close to those of the WDs. Here we attempt to address this question. Following a suggestion by the referee, we have chosen a subset of the images in the Hubble Ultra Deep Field (HUDF; Beckwith et al. 2006), in which practically all detected objects should be galaxies. The suggestion was that we choose a set of images with a total exposure similar to what we had in NGC 6791, and measure them in the same way.

Unfortunately the HUDF observations did not include the F814W filter; the closest filters to it were F775W and F850LP. We chose to work with F775W, because it is easier to transform into the F814W band. The throughputs of F775W and F814W are close enough that we felt that we could simply match the total exposure times. The HUDF images used here thus consist of 6 × 1200 s exposures in F606W, and 12 × 1200 s in filter F775W.

The reduction, selection of objects, calibration, and analysis were done in exactly the ways described in the previous sections, except that we used unperturbed library PSFs. The RADXS parameter seemed to do an extremely good job of rejecting the

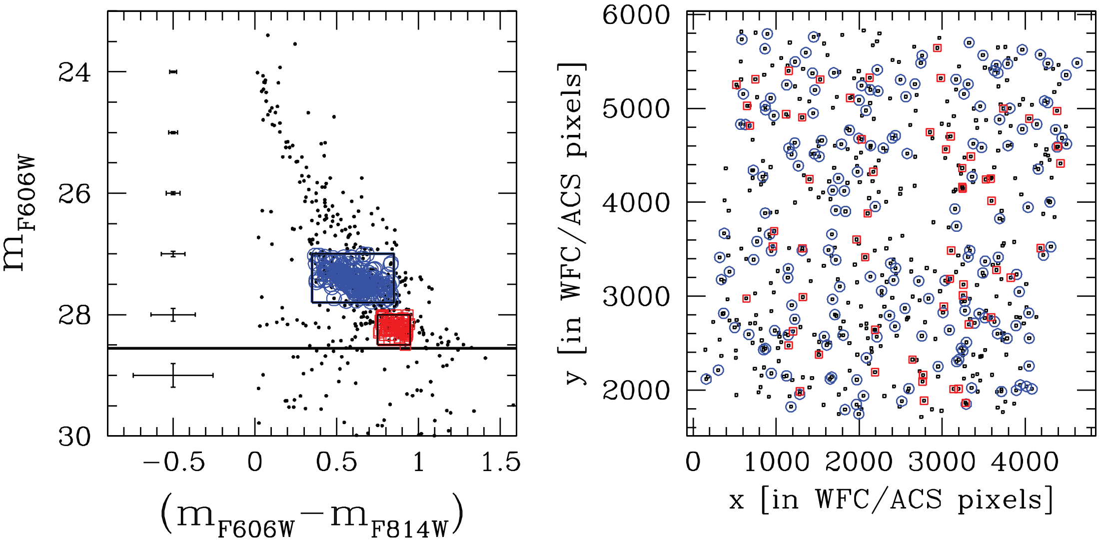

Fig. 8.—*Left*: CMD of the WD region, with the completeness limit marked. The error bars show the photometric errors in magnitude and color, as a function of magnitude. The two boxes delimit the areas that we took as representative of the two LF peaks. *Right*: Spatial distributions of objects. The black dots are all those above the completeness limit. On both sides objects belonging to the brighter peak are marked in blue (*circles*), and those belonging to the fainter peak in red (*squares*).

nonpointlike sources. We did not make AS runs on the HUDF images, however, because we did not consider it to be necessary in this rough exercise. We simply assume that because the total exposure was chosen to be similar, objects that are at the completeness limit in (F606W, F814W) will also be close to the completeness limit in (F606W, F775W).

In the HUDF essentially all objects are galaxies. In the upper part of Figure 9 we present (on a more compressed color scale) CMDs for the objects in the HUDF across all the various selection stages, exactly as in the top panels of Figure 3, but with the F775W filter instead of F814W. Note how the galaxies that have slipped through our selection process are nearly all confined to a narrow triangular plume extending up from our completeness limit.

In the lower half of the figure is shown a portion of the CMD. On the left is the HUDF CMD in its color system, and on the right the NGC 6791 CMD in its color system. We drew in the HUDF CMD a triangle extending downward to an arbitrary but generously faint baseline; it is shown by heavy lines. The symbols (*small triangles*) within the triangle represent the HUDF objects that met all our stellar criteria. Adjacent to the right edge of the triangle are theoretical WD isochrones (which will be discussed in § 8.1) in the color system of this CMD. Since the later discussion will show that they fall in the region of the WDCS, it is clear that our triangle falls close to where the WD sequence should lie.

We then transformed the vertices of this triangle into the magnitude system of the NGC 6791 CMD. To do this we used the transformations from *HST* filters to Johnson-Cousins (*V*, *I*) given by Sirianni et al. (2005); next we used the Sirianni relations to transform from (*V*, *I*) to (F606W, F814W). (Note: As the Sirianni procedures are set up, the transformation from *HST* filters to Johnson-Cousins requires an iterative process, whereas the transformation back to a *HST* system requires only a direct evaluation.) The triangle as transformed into the NGC 6791 system also required applying the interstellar absorption, for which we assumed 0.47 mag in F606W and 0.31 mag in F814W, in agreement with the absorption and reddening used elsewhere in this paper. The same isochrones are repeated here, but in the color system of this CMD and with the same adjustments for absorption.

We transformed not only the vertices of the triangle, but also the HUDF objects that lay within it. We then truncated this triangle at our completeness limit, $m_{\rm F606W} = 28.55$. Within the remaining area, the lower right panel of the figure shows the triangle, and within it the NGC 6791 stars in light gray and the transformed HUDF objects in dark gray. (The HUDF objects below the completeness limit are plotted as tripointed asterisks; they were excluded from the discussion that follows.)

One conspicuous difference is that the HUDF objects extend to a noticeably bluer color. In trying to understand this, we note that the HUDF objects are nonstellar, whereas we have used color transformations that are appropriate only for stars. Since we do not know the spectral energy distributions (SEDs) of these objects, the difference could be due to having used stellar SEDs rather than the correct but unknown ones. Because the NGC 6791 objects extend continuously across the right edge of the triangle as it is shown, the number of them that fall within the triangle is obviously quite sensitive to the color transformation, and is therefore rather uncertain. What the lower right panel does make clear, however, is that it is highly likely that a significant number of NGC 6791 objects on the blue side of the WDCS are likely to be the nuclei of background galaxies.

In any case, and most importantly, we note that the number of objects in question is small—at most a few dozen. This means that this source of possible contamination cannot be responsible for the second peak in the WD LF, nor for the discrepancy between the predicted and observed numbers of WDs that was noted in § 6.

8. THEORETICAL IMPLICATIONS

Our new luminosity function (LF) of the white dwarfs (WDs) in NGC 6791 confronts us with two theoretical problems:

1. The LF has two distinct peaks, rather than a single one.
2. Fitting either peak with a theoretical LF calculated from conventional WD cooling theory leads to a WD age that is smaller than the age derived from the main-sequence TO. (We showed this for the brighter peak in Bedin et al. [2005a]. We will confirm this discrepancy below, and will show that it exists even if we fit the fainter peak instead.)

In this section we will explore ways in which conventional theory might be modified in order to cope with these two problems.

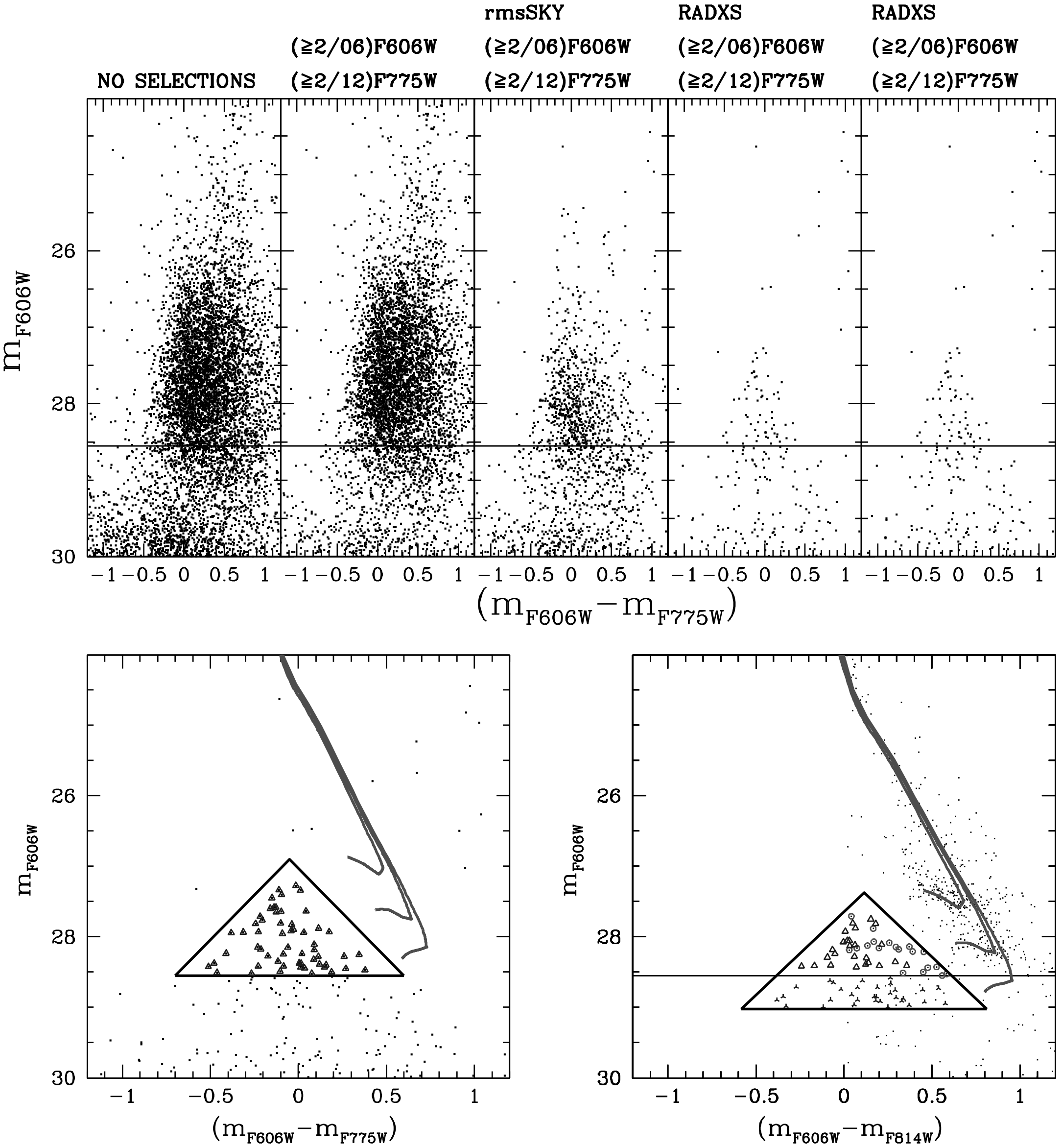

Fig. 9.— *Top*: Same as in top panel of Fig. 3, but for the HUDF. *Bottom left*: Faint part of WD region of CMD, in HUDF, with F775W for *I* filter. *Bottom right*: Same, but for NGC 6791, with F814W for *I* filter. For the meaning of the lines, triangles, and highlighted stars, see text. [*See the electronic edition of the Journal for a color version of this figure.*]

8.1. *Fitting with the Conventional Theory*

We have calculated WD isochrones and LFs with [Fe/H] = 0.40 for the WD progenitors (following the most recent spectroscopic estimates by Gratton et al. [2006], Carraro et al. [2006], and Origlia et al. [2006]). All models and isochrones are from the BaSTI database (Pietrinferni et al. 2004), and the Salaris et al. (2000) WD tracks have been transformed into the ACS WFC Vegamag system as described in Bedin et al. (2005b). The adopted CO profiles of our WD models are from Salaris et al. (1997). The initial-final mass relationship is from Ferrario et al. (2005), extrapolated linearly for initial masses below 2.5 $M_\odot$ (i.e., below the lower M_i limit of the Ferrario et al. determination). The relationship implies that $M_f = 0.53\ M_\odot$ at $M_i = 1.0\ M_\odot$. As a test, we also examined the different M_i-M_f relationship used in the Richer et al. (2000) WD isochrones, and in Kalirai et al. (2008), but the results we obtain are virtually the same.

The [Fe/H] = 0.40 isochrones have been used to fit our *HST* results; we derived $E(B-V) = 0.17$, $(m-M)_V = 13.50$, and a TO age of about 8 Gyr. A fit to our *HST* CMD employing these values for reddening and distance modulus is displayed in the upper panels of Figure 10, for both the TO and the WDs. For reference, this distance modulus requires an age of ~6 Gyr (about 2 Gyr younger than the TO age) to reproduce the WDLF peak at $m_{\rm F606W} \sim 28.2$, or an age of ~4 Gyr (~4 Gyr younger than the TO age) to reproduce the peak at $m_{\rm F606W} \sim 27.4$, as also shown in the lower panel of Figure 10.

Even though the ages associated with these fits are presumably wrong, we note that each of them does reproduce the observed hook toward the blue and toward brighter magnitudes. This hook is caused by the more massive objects (coming from higher mass progenitors) that pile up at the bottom of the WD isochrone, moving the track in the blue direction because these higher mass WDs have smaller radii. It is important to note that this blue hook has nothing to do with the blueward turn of the individual cooling sequences of WDs with H atmospheres, caused by strong absorption from H_2 in the infrared (Hansen 1998; Saumon & Jacobson 1999).

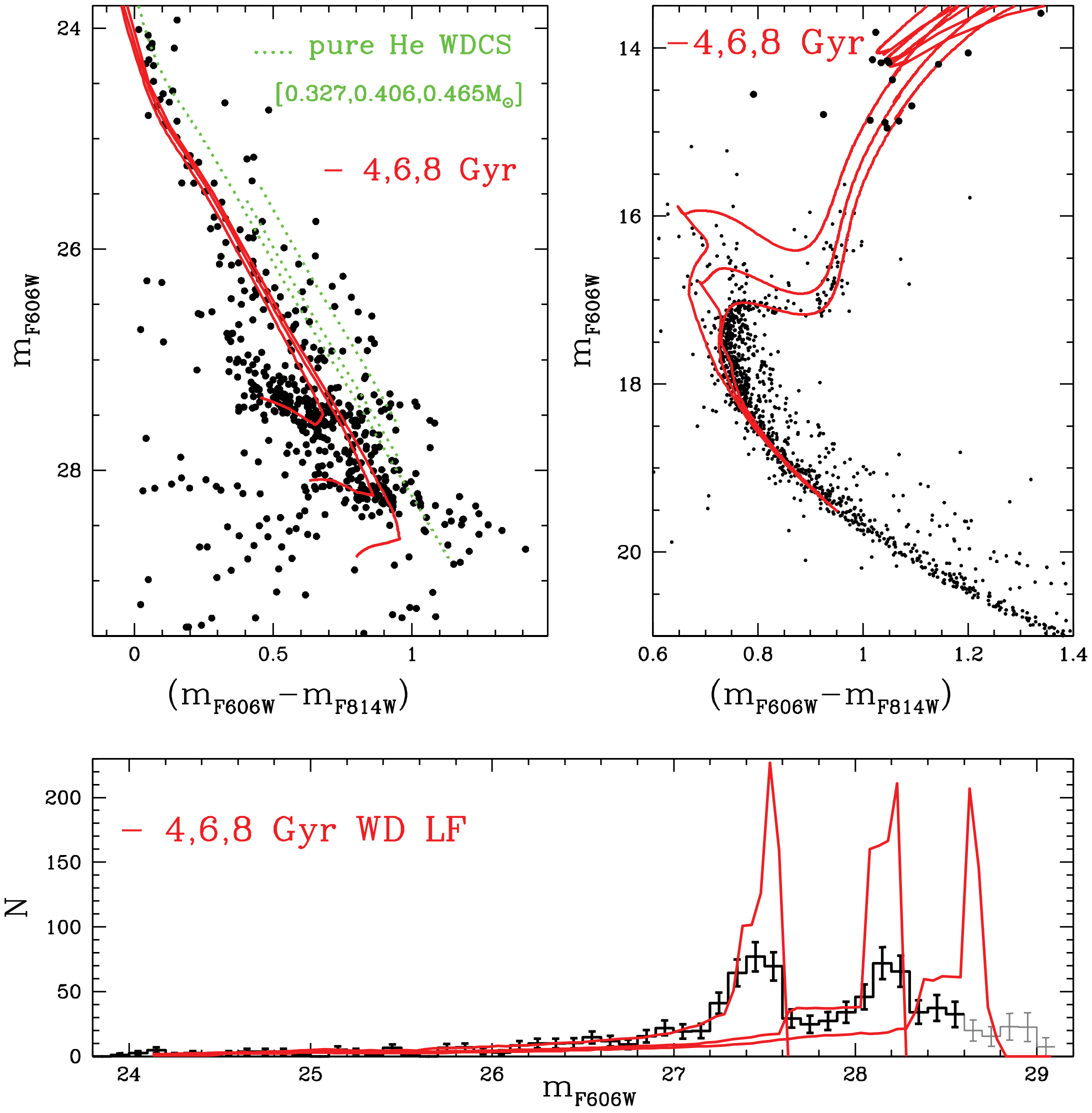

Fig. 10.—Fit of theoretical isochrones and LFs of CO WDs for ages 4, 6, and 8 Gyr to the observed CMD of NGC 6791 and to the WD star counts (see text for details). Auxiliary quantities used here are $E(B-V)=0.17$, $(m-M)_V=13.5$, $R_V=3.2$, $A_{F606W}=0.47$, and $A_{F814W}=0.31$. Cooling sequences of He WDs with masses equal to, respectively, 0.327, 0.406, and 0.465 $M_\odot$ are also displayed (the bluest being the most massive). Note that no normalization of the theoretical LFs to the observed numbers has been attempted, as the only purpose of the comparison in the lower panel is to show the expected position in magnitude of the peaks for the different assumed ages.

That H_2-induced turn to the blue sets in only when the $T_{\rm eff}$ of the models reaches below ~4000 K, whereas the coolest temperature reached by the observed WDs is ~5400 K, according to our 6 Gyr WD isochrone, which matches the faint end of the observed sequence. We also note that some WDs belonging to the brighter peak of the LF seem to extend farther to the blue than the 4 Gyr isochrone does, and to even brighter magnitudes.

8.2. *White Dwarf Cooling Times*

In any case, the discrepancies between these WD ages and the age derived from MS TO stars constitute a serious conflict. There must be some significant error either in the models that fit the TO (which seems unlikely) or in the models that fit the WD cooling sequence. We now look for ways to make our theoretical WDs cool more slowly.

One possible way of slowing the cooling of WDs is to change the relative abundances of C and O. The recent Kunz et al. (2002) estimate of the $^{12}C(\alpha,\gamma)^{16}O$ reaction rate is only about 2/3 of the Caughlan et al. (1985) rate employed to compute the evolutionary CO profiles of the Salaris et al. (2000) WD models. This lower rate would produce a C/O ratio in the core of WDs that is closer to unity compared with our adopted models. This would, in turn, increase the delay introduced by the CO separation on crystallization. Taking advantage of the analyses of Montgomery et al. (1999) and Isern & García-Berro (2000), we estimate that the extra delay in the cooling process would be in any case less than 1 Gyr at the luminosities corresponding to the two observed peaks [$\log(L/L_\odot)\sim -3.7$ and ~ -4.0].

An additional effect that could slow down the cooling process is the diffusion of ^{22}Ne in the liquid phase. The Ne abundance should be about 4% by mass, and its diffusion is not included in any of the existing large WD model grids. Calculations by Deloye & Bildsten (2002) show that the delays produced by this process are ~1 Gyr for the NGC 6791 WDs. Very recent calculations by Garcia-Berro et al. (2008) do not change this picture appreciably, if one makes the most realistic assumptions about the ^{22}Ne diffusion coefficient, carbon and oxygen stratification, and crystallization process.

A third process that could potentially add an extra delay to the WD cooling timescales is the ^{22}Ne separation during the crystallization phase (Segretain et al. 1994). Our adopted WD models include only the effect of separation of a CO binary mixture, without taking into account the presence of a small amount of ^{22}Ne. Segretain (1996) computed the phase diagram of a ternary C/O/Ne mixture, and estimated an extra delay of ∼0.4 Gyr due to Ne separation, for a 1% Ne mass fraction in the WD core. This delay would affect the theoretical WD isochrones and LFs only marginally; however, one needs computations of this effect for a larger Ne abundance typical of NGC 6791 WDs, and more realistic CO profiles (Segretain [1996] consider a flat C and O profile, with 49.5% mass fraction each), before drawing definitive conclusions about the relevance of this process.

The effect of one or more of these processes might allow isochrones of a reasonable age to fit the fainter peak, but it is very difficult, if not impossible, to reproduce the brighter one. In any case, we would be ignoring the glaring problem of having two distinct peaks in the WDLF.

8.3. *Helium White Dwarfs*

An obvious way of dealing with the two peaks in the WD LF is to assume that the cluster has two different kinds of WDs, and a reasonable hypothesis would be that in addition to the usual CO WDs the cluster has a population of WDs whose cores consist of helium.

In fact, Hansen (2005) has put forward the idea that the bright peak at $m_{\rm F606W} \sim 27.4$ is caused by massive helium WDs, produced by red giant branch (RGB) stars that just missed He ignition (because of mass loss due to stellar winds). This idea is supported by the fact that NGC 6791 contains a nonnegligible number of blue He-burning stars that have very little mass in their envelopes, having lost nearly all of the envelope during their RGB lives. Kalirai et al. (2007) have recently estimated the masses of several objects along the bright part of the WD sequence and conclude that a substantial fraction of the NGC 6791 WDs are actually helium WDs. Given that He WDs cool down more slowly than CO WDs, an ad hoc choice of the relationship between the mass (and number) of RGB stars that have lost all their envelope before the He ignition, on the one hand, and the final He WD mass, on the other hand, can produce a LF that reproduces the bright observed peak for an age compatible with the TO age (Hansen 2005).

A serious problem with this scenario is that the He core mass at the He flash is 0.46 $M_\odot$ at the supersolar metallicity of NGC 6791 (Pietrinferni et al. 2004). Even at solar metallicity it is just 0.47 $M_\odot$. We have therefore computed the evolution of a 0.465 $M_\odot$ He WD using the code by Serenelli et al. (2002). The color transformations applied to this model are the same as for the CO WD isochrones. The top left panel of Figure 10 displays this sequence (*green dotted line*) together with additional He WD models of lower mass, already shown in Bedin et al. (2005a). These low-mass models overlap with objects redder than the main body of the cooling sequence, which most likely correspond to the fainter counterpart of the bright He WDs identified by Kalirai et al. (2007). As for the 0.465 $M_\odot$ track, this is too red by ∼0.08 mag in ($m_{\rm F606W} - m_{\rm F814W}$) compared to the main branch of the CO isochrone that reproduces very well the main body of the observed cooling sequence. One would need He WDs above ∼0.5 $M_\odot$ to eliminate this discrepancy. Another important issue is whether He core WDs are able to reproduce the objects along the blue hook corresponding to the bright peak in the LF. We stress again that the $T_{\rm eff}$ of both CO and He core WDs at these magnitudes are both well above 4000 K; therefore, one cannot invoke the turn to the blue caused by H_2 absorption (which in any case is included in our adopted color transformations) to explain the observed blue hook in terms of single-mass cooling sequences. Thus for the case of He WDs this feature can be caused only by the presence of a range of masses that has to extend above 0.5 $M_\odot$.

As an extreme test, one could in principle disregard the fit to the MS, the TO, and the RGB, and consider only the observed WD sequence. Assuming $E(B-V) = 0.09$–0.10, the lowest reddening among the values quoted in the literature (see Stetson et al. 2003), the 0.465 $M_\odot$ He WD track overlaps with the main body of the cooling sequence—with this $E(B-V)$ value, the MS and RGB would not be matched by theoretical models—but obviously fails to match the blue hook. To reproduce this feature (leaving aside the resulting values of the cooling age and the TO age) one has to unrealistically increase the cluster distance modulus by ∼1 mag—i.e., $(m-M)_V \sim 14.5$, which corresponds to $(m-M)_0 \sim 14.2$ for $E(B-V) = 0.09$–0.10—so that the 0.465 $M_\odot$ model would intersect the bluest point along the blue hook, and lower masses would progressively shift toward the red side of the hook. Even before considering the adequacy of the resulting cooling ages, one has to note that such a large distance modulus is well outside the range of all reasonable determinations (Stetson et al. 2003). Again the conclusion is that He core WDs with a spectrum of masses extending well beyond 0.5 $M_\odot$ are necessary if one wants to explain the observed bright peak of the LF in terms of these objects.

One physical mechanism that could produce massive He WDs is rotation. Mengel & Gross (1976) showed that rotation can increase the value of the core mass at the He flash by as much as 0.15 $M_\odot$ of a solar mass, compared with standard nonrotating models. As a general rule, when the angular momentum transport mechanism is fixed, faster rotating stars will reach larger core masses at the time of He flash. As a by-product, according to the Reimers (1975) mass-loss law, rotating stellar models lose more mass when approaching the He flash compared with nonrotating or slowly rotating ones. This provides a natural mechanism that favors the production of blue He-burning objects (extreme blue HB, as observed in this cluster) and massive He WDs (which might explain the brighter peak of the WDLF). Stellar rotation causes a broadening of the lower part of the RGB (Brown 2007). Curiously enough, this broadening of the base of the RGB (broader than expected from observational errors) seems to be present in the CMDs from Stetson et al. (2003; see their Fig. 17), Bruntt et al. (2003; see their Figs. 2, 3, 5, and 10), and in our own CMD. Note that this RGB broadening cannot be due to a spread in metallicity, as Carraro et al. (2006) find a negligible (±0.01 dex) dispersion in [Fe/H]. In addition, extra mixing induced by rotation of the stars (Charbonnel 1995 and references therein) leads to a low value of ^{12}C/^{13}C, as observed by Origlia et al. (2006) in RGB stars of NGC 6791.

We are currently investigating (D. Brown et al. 2008, in preparation) what initial rotation rates and angular momentum transport prescriptions are necessary to produce He core masses ∼0.5 $M_\odot$ and higher at the metallicity of NGC 6791, the impact of rotation on the theoretical CMD, and the corresponding predicted surface rotation velocities along the CMD. This investigation, together with spectroscopic measurements (presently lacking) of surface rotation of MS and TO stars, may definitively prove or disprove this scenario.

J. A. and I. R. K. acknowledge support from STScI grants GO-9815 and GO-10471. We thank Alvio Renzini for many useful discussions. We warmly thank Lars Bildsten and Christopher Deloye for valuable discussions about ^{22}Ne. We also thank the anonymous referee for the careful reading and for useful suggestions. A. S. is a John Bahcall Fellow at the IAS.

REFERENCES

Anderson, J., & King, I. R. 2006, PSFs, Photometry, and Astronomy for the ACS/WFC (Instrum. Sci. Rep. ACS 2006-01; Baltimore: STScI) (AK06)

Anderson, J., et al. 2008, AJ, submitted

Beckwith, S. V. W., et al. 2006, AJ, 132, 1729

Bedin, L. R., Cassisi, S., Castelli, F., Piotto, G., Anderson, J., Salaris, M., Momany, Y., & Pietrinferni, A. 2005b, MNRAS, 357, 1038

Bedin, L. R., Piotto, G., Carraro, G., King, I. R., & Anderson, J. 2006, A&A, 460, L27

Bedin, L. R., Salaris, M., Piotto, G., King, I. R., Anderson, J., Cassisi, S., & Momany, Y. 2005a, ApJ, 624, L45

Brown, D. 2007, Ph.D. thesis, Liverpool John Moores Univ.

Bruntt, H., Grundahl, F., Tingley, B., Frandsen, S., Stetson, P. B., & Thomsen, B. 2003, A&A, 410, 323

Carraro, G., Villanova, S., Demarque, P., McSwain, M. V., Piotto, G., & Bedin, L. R. 2006, ApJ, 643, 1151

Caughlan, G. R., Fowler, W. A., Harris, M. J., & Zimmermann, B. A. 1985, At. Data Nucl. Data Tables, 32, 197

Charbonnel, C. 1995, ApJ, 453, L41

Deloye, C. J., & Bildsten, L. 2002, ApJ, 580, 1077

Ferrario, L., Wickramasinghe, D., Liebert, J., & Williams, K. A. 2005, MNRAS, 361, 1131

Fruchter, A. S., & Hook, R. N. 2002, PASP, 114, 144

García-Berro, E., Althaus, L. G., Córsico, A. H., & Isern, J. 2008, ApJ, 677, 473

Gratton, R., Bragaglia, A., Carretta, E., & Tosi, M. 2006, ApJ, 642, 462

Hansen, B. M. S. 1998, Nature, 394, 860

———. 2005, ApJ, 635, 522

Isern, J., & García-Berro, E. 2000, ApJ, 528, 397

Kalirai, J. K., Bergeron, P., Hansen, B. M. S., Kelson, D. D., Reitzel, D. B., Rich, R. M., & Richer, H. B. 2007, ApJ, 671, 748

Kalirai, J. K., Hansen, B. M. S., Kelson, D. D., Reitzel, D. B., Rich, R. M., & Richer, H. B. 2008, ApJ, 676, 594

King, I. R., Bedin, L. R., Piotto, G., Cassisi, S., & Anderson, J. 2005, AJ, 130, 626

Kroupa, P. 2001, MNRAS, 322, 231

Kunz, R., Fey, M., Jaeger, M., Mayer, A., Hammer, J. W., Staudt, G., Harissopulos, S., & Paradellis, T. 2002, ApJ, 567, 643

Mengel, J. G., & Gross, P. G. 1976, Ap&SS, 41, 407

Montgomery, M. H., Klumpe, E. W., Winget, D. E., & Wood, M. A. 1999, ApJ, 525, 482

Origlia, L., Valenti, E., Rich, R. M., & Ferraro, F. R. 2006, ApJ, 646, 499

Pietrinferni, A., Cassisi, S., Salaris, M., & Castelli, F. 2004, ApJ, 612, 168

Reimers, D. 1975, Mem. Soc. R. Sci. Liège, 8, 369

Richer, H. B., Hansen, B., Limongi, M., Chieffi, A., Straniero, O., & Fahlman, G. G. 2000, ApJ, 529, 318

Riess, A., & Mack, J. 2004, Time Dependence of ACS WFC CTE Corrections for Photometry and Future Predictions (Instrum. Sci. Rep. ACS 2004-06; Baltimore: STScI)

Salaris, M., Dominguez, I., García-Berro, E., Hernanz, M., Isern, J., & Mochkovitch, R. 1997, ApJ, 486, 413

Salaris, M., García-Berro, E., Hernanz, M., Isern, J., & Saumon, D. 2000, ApJ, 544, 1036

Saumon, D., & Jacobson, S. B. 1999, ApJ, 511, L107

Segretain, L. 1996, A&A, 310, 485

Segretain, L., Chabrier, G., Hernanz, M., García-Berro, E., Isern, J., & Mochkovitch, R. 1994, ApJ, 434, 641

Serenelli, A. M., Althaus, L. G., Rohrmann, R. D., & Benvenuto, O. G. 2002, MNRAS, 337, 1091

Sirianni, M., et al. 2005, PASP, 117, 1049

Stetson, P. B., Bruntt, H., & Grundahl, F. 2003, PASP, 115, 413